Spin semimetallic behavior and sublattice spin crossover in the fully compensated ferrimagnetic half-Heusler compound $(Co_{0.5}Mn_{0.5})MnAl$

R. Harikrishnan,[1,*] Jatin Kumar Bidika,[2,3] B. R. K. Nanda,[2,3] Arout J. Chelvane,[4] S. D. Kaushik,[5] P. D. Babu,[5] and Harish Kumar Narayanan[1,*]

[1]*Advanced Magnetic Material Laboratory, Department of Physics, Indian Institute of Technology-Madras, Chennai 600036, India*

[2]*Condensed Matter Theory and Computational Laboratory, Department of Physics, Indian Institute of Technology Madras, Chennai 600036, India*

[3]*Centre for Atomistic Modelling and Materials Design, Indian Institute of Technology Madras, Chennai 600036, India*

[4]*Defense Metallurgical Research Laboratory, Kanchan Bagh (PO), Hyderabad 500058, India*

[5]*UGC-DAE Consortium for Scientific Research, Mumbai Center, R-5 shed, BARC, Trombay, Mumbai 400085, India*

(Received 31 December 2022; revised 20 July 2023; accepted 10 August 2023; published 5 September 2023)

We experimentally demonstrate rarely observed fully compensated ferrimagnetic behavior in the half-Heusler compound $(Co_{0.5}Mn_{0.5})MnAl$. A comprehensive structural investigation at room temperature was carried out using x-ray and neutron diffraction techniques, which indicated that the sample exhibited a $C1_b$ structure with B2-type disorder. The magnetic measurement on this compound reveals that the sample has a completely compensated ferrimagnetic behavior with a very low saturation magnetization of 0.09 μ_B/f.u. and a Curie temperature of 634 K. This finding was further verified by neutron diffraction techniques. Around 200 K, a change in the sign of the magnetic moment and anomalous Hall resistivity was observed, resulting from sublattice spin crossing. The resistivity measurement indicates an unusual temperature dependence with a negative temperature coefficient, revealing the possibility of alternative mechanisms for electronic transport observed in materials such as semimetals or gapless/spin-gapless semiconductors. The compensated ferrimagnetic behavior is analyzed and substantiated by carrying out fixed spin moment calculations within the framework of density functional theory. The electronic structure analysis predicts a spin semimetallic quantum phase for this half-Heusler compound.

DOI: 10.1103/PhysRevB.108.094407

I. INTRODUCTION

Authors of recent *ab initio* studies and experimental reports have suggested the possible existence of a spintronic material known as a spin semimetal (SSM) [1]. These are materials that have one semimetallic spin band and one that is either insulating or semiconducting. The SSM band is made up of two or more distinct types of valence and conduction bands that partially overlap, leading to a finite density of states (DOS) in the SSM band at the Fermi level (E_F). Heusler compounds continue to remain in focus in the field of spintronics due to the discovery of a wide variety of strongly spin-polarized materials with peculiar band structures such as half-metallic ferromagnets, half-metallic ferrimagnets, half-metallic fully compensated ferrimagnets (FCFMs), spin-gapless semiconductors, and SSMs. Among the various Heusler compounds with high spin polarization, FeRhCrGe [1] has been found to exhibit SSM characteristics. This was followed by CoFeVSb [2] and the theoretical prediction of Mn_2LiGa [3]. Similarly, theoretical calculations have predicted SSM characteristics in some half-Heusler compounds, including CoMnSe, PtCrP, and CoCrAl/Ga [4]. Even though these materials exhibit SSM characteristics, their large magnetic moment is undesirable for spintronic applications, as the stray fields produced by these materials may affect the performance of devices. Hence, there is a search for ferrimagnetic materials with high spin polarization but very low magnetic moments. In cubic Heusler compounds of the structural types $L2_1$ and $C1_b$, the total magnetic moment per formula unit is defined by the Slater-Pauling (S-P) rule as follows: $m = Z_t - 24$ for $L2_1$ and $m = Z_t - 18$ for $C1_b$. Here, Z_t indicates the total number of valence electrons per unit cell [5,6]. As a result, neither half-Heusler compounds with $Z_t = 18$ nor full-Heusler compounds with $Z_t = 24$ will have a macroscopic magnetic moment. These materials are known as half-metallic FCFMs [7]. Some of the unique advantages of FCFMs are (1) the virtually negligible magnetic moment results in no external stray fields and hence reduced energy losses; (2) spin sensitivity with no stray magnetic fields, allowing them not to affect the spin character and making them excellent for spin-polarized scanning tunneling microscope tips and improved circuit integration density in a chip [8,9]; (3) low shape anisotropy, which aids in applications such as spin injection; (4) the faster dynamics of these materials over ferromagnets make them appropriate for the fabrication of high-speed electronic devices in the terahertz region [10,11]; and (5) FCFMs were also projected to serve as the foundation for a class of superconductors known as a single-spin superconductors which have just one superconducting spin channel [12]. These characteristics make them preferable to half-metallic ferromagnets, and they are in high demand today. The SSM property along with FCFM was recently predicted theoretically in the inverse Heusler compound Mn_2LiGa [3] but has yet to be confirmed experimentally.

*nhk@iitm.ac.in

The antisite disorder is more common in full-Heusler compounds than in half-Heusler compounds, according to theoretical studies [13]. As a result, half-Heusler compounds are preferred over full-Heusler compounds for achieving the FCFM state via substitution. Half-Heusler compounds are more likely to have a larger band gap in one of their spin bands than full-Heusler compounds. Furthermore, it has been found via several studies that half-Heusler compounds can only be stable with 18 or with $18 + 4f^n$ valence electrons when rare-earth elements are added [13]. Consequently, a magnetic half-Heusler having 18 valence electrons offers two significant advantages: extraordinary stability and FCFM. It is worth mentioning that most Heusler-based FCFMs contain Mn, which is an inevitable element in the formation of ferrimagnetism and band gap in half-Heusler compounds [14]. Therefore, Mn-based half-Heusler compounds having $Z_t = 18$ will be promising choices for FCFMs. This property was predicted in the half-Heusler compound MnCrSb by de Groot [8]. Subsequently, half-Heusler compounds such as FeMnGa/Al/In [14], $Mn_2Si_{1-x}Ge_x$ [15], Mn_2Sn [16], and Cr_2Se [17] have been predicted to exhibit FCFM properties by *ab initio* studies. However, none of these compounds were crystallizing in the desired $C1_b$ structure. There has not yet been any theoretical or experimental realization of FCFM-SSMs in the half-Heusler family.

Based on theoretical calculations, Ma *et al.* [18] predicted the coexistence of a ferrimagnetic ground state with a magnetic moment of 1 μ_B/f.u., as predicted by the S-P rule, and a pseudogap near the E_F, in the cubic half-Heusler compound CoMnAl. Magnetic moment compensation is feasible in CoMnAl by modulating the number Z_t by substituting Mn at the Co site. Using the S-P rule on the CoMnAl system, we can find that Z_t for the composition $(Co_{0.5}Mn_{0.5})$MnAl will be 18. Hence, this material will be a good candidate in the quest for FCFMs in the half-Heusler system. We synthesized this compound and investigated its structural, magnetic, and electrical transport characteristics experimentally, which revealed the coexistence of SSM properties and FCFM behavior in this material. Furthermore, the fixed spin moment (FSM) results obtained from density functional theory (DFT) calculations on ordered $(Co_{0.5}Mn_{0.5})$MnAl agree well with the above findings.

II. EXPERIMENTAL DETAILS

The preparation of polycrystalline $(Co_{0.5}Mn_{0.5})$MnAl was done by arc melting high pure constituent elements. The elements were weighed as per the stoichiometric proportions, and owing to the volatility of manganese, an extra 3% was added to make up for the weight loss caused by the melting process. Prior to melting the elements, a titanium getter was melted to remove any traces of oxygen present in the chamber. The ingot was melted multiple times after flipping it to achieve homogeneity. The structural analysis was carried out using Cu-$K\alpha$ radiation ($\lambda = 1.5418$ Å) employing a Rigaku Smart Lab high-resolution x-ray diffractometer. Powder neutron diffraction (PND) was performed on the Focussing Crystal based diffractometer (PD-3) installed by UGC-DAE CSR at Dhruva reactor, BARC Mumbai by employing a neutron beam of wavelength 1.48 Å. The measurement was performed on a powdered sample that was placed in a cylindrical vanadium sample container due to its extremely low coherent scattering length. Employing the FULLPROF Rietveld refinement software suite, the analysis of both diffraction data was done. Using the Apreo-S scanning electron microscope, the phase purity and composition of the sample were evaluated by backscattered electron (BSE) imaging and energy dispersive x-ray (EDX) spectroscopy, respectively. Magnetic measurements were carried out with the Quantum Design MPMS 3 SQUID VSM in the low-temperature regime and the Lake Shore VSM in the high-temperature regime. Four-probe electrical resistivity, Hall resistivity, and Seebeck coefficient were measured employing a physical property measurement system (PPMS-Dynacool; Quantum Design).

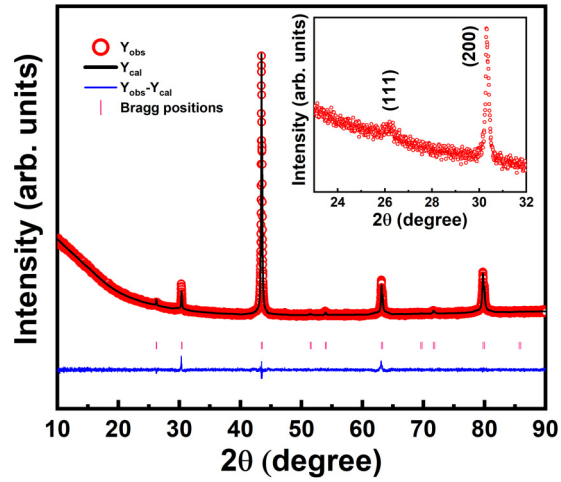

FIG. 1. X-ray diffraction (XRD) data of $(Co_{0.5}Mn_{0.5})$MnAl measured at room temperature along with the Rietveld refinement fit.

III. RESULTS AND DISCUSSIONS

A. Experimental results

1. Structural properties

Figure 1 depicts the x-ray diffraction (XRD) data of the $(Co_{0.5}Mn_{0.5})$MnAl compound [using Cu-$K\alpha$ radiation ($\lambda = 1.5418$ Å)]. Low-angle reflections like (111) and (200), as well as the order-independent reflections (220), (400), and (422), would be present in a completely ordered cubic half-Heusler structure ($C1_b$). The existence of the peaks (111) and (200) allows for the distinction of the degree of ordering of the half-Heusler compounds. Although the diffraction pattern of this sample shows both order-dependent reflections like (111) and (200) (see inset of Fig. 1), the strength of the (111) peak was found to be less intense. A possible explanation for the decrease in the strength of these superlattice reflections might be owing to identical x-ray scattering factors for Mn and Co atoms. Another possibility is the occurrence of B2-type antisite disorder in half-Heusler systems [13]. Based on the structural configuration of CoMnAl considered in the total energy calculation done by Ma *et al.* [18], the $C1_b$ structure of $(Co_{0.5}Mn_{0.5})$MnAl can be considered as three interpenetrating face-centered cubic sublattices with Al atoms occupy the 4*a* position, whereas Co atoms occupy the 4*c* position. Mn atoms,

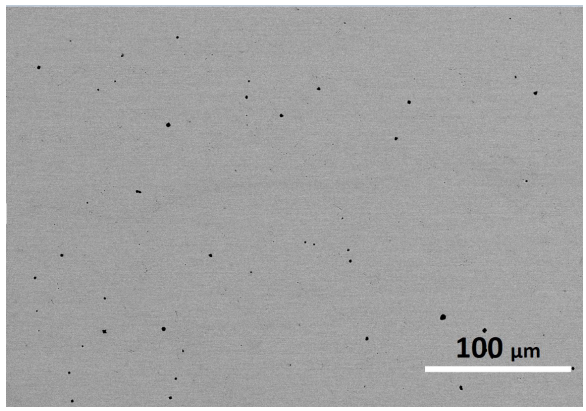

FIG. 2. Backscattered electron image of $(Co_{0.5}Mn_{0.5})$MnAl. Small pores on the surface of the sample are shown by black spots.

on the other hand, occupy two distinct Wyckoff positions. The first Mn (Mn_I) replaced at the Co site is at 4*c*, whereas the second Mn (Mn_{II}) is at 4*b*, and the 4*d* site is vacant. Moreover, the lattice parameter was estimated using Rietveld refinement of XRD data within the FULLPROF suite, assuming the $C1_b$ structural configuration mentioned above, and was found to be $a_{exp} = 5.87$Å. The powder XRD pattern, along with the Rietveld refinement fit, is shown in Fig. 1.

The compositional analysis was carried out with the help of EDX spectroscopy. The average composition calculated by spot EDX spectrum taken at different regions shows the stoichiometry as $Mn_{1.48}Co_{0.47}Al_{0.98}$, which is very close to the required stoichiometry. The BSE image revealed that the material has formed in single phase with no traces of any secondary phase (Fig. 2).

2. *Magnetic properties*

Figure 3(b) depicts the *M* (*T*) curve measured for $(Co_{0.5}Mn_{0.5})$MnAl in various fields. The *M*-*T* graph in a field of 100 Oe [Fig. 3(a)] exhibits unique magnetic behavior, with a Curie temperature (T_C) of 634 K. Below T_C, magnetization falls and reaches a minimum at ∼ 260 K, then increases as the temperature lowers. This is characteristic of an N-type ferrimagnetic system with a compensation temperature (T_{com}) of 260 K. However, it is interesting that the *M*-*T* measurements at comparatively high fields, such as 500 and 70 kOe, show similar N-type ferrimagnetic behavior with a variation in the T_{com}, as depicted in Fig. 3(b). The most noticeable macroscopic aspect of ferrimagnetism is the formation of distinct shapes for the temperature dependence of spontaneous magnetization curves, such as R-, P-, and N-type ferrimagnetic orders [19]. Among these various types of ferrimagnetic ordering, the N type has the most characteristic dependency, in which the sign of spontaneous magnetization reverses at T_{com}. Hence, as seen in Fig. 3(b), magnetic measurements were carried out at relatively low fields in the temperature range of 5–300 K, and the measurements were carried out on tiny pieces of the sample to prevent relative reorientation of the grains [20]. Furthermore, the measurements were carried out after nullifying the negative trapped field of the SQUID-based VSM with an ultralow field probe. As expected, the *M*-*T* curve at the low field reveals a magnetization reversal, as shown in Fig. 3(b). In this measurement, both zero-field-cooled and field-cooled curves with negative values at high temperatures cross the temperature axis at 201, 213, and 224 K, corresponding to the fields 10, 20, and 50 Oe, respectively, and turn positive as the temperature decreases further. This crossover demonstrates the presence of sublattice magnetic compensation in the system. Other Heusler compounds, such as $Mn_{1.5}V_{0.5}$FeAl [21] and Mn_2Ru_xGa [22], show similar N-type ferrimagnetic behavior and magnetic crossover. However, $(Co_{0.5}Mn_{0.5})$MnAl exhibits a significant field dependence on T_{com}, in contrast to other Heusler-based compensated ferrimagnets like $Mn_{1.5}V_{0.5}$FeAl [21]. It is worth noting that the observed $T_{com}(= 260\,K)$ for $(Co_{0.5}Mn_{0.5})$MnAl at 100 Oe is significantly greater than that of $Mn_{1.5}V_{0.5}$FeAl [21] and Mn_2Ru_xGa [22].

The total magnetic moment per formula unit (μ_B/f.u.) for $(Co_{0.5}Mn_{0.5})$MnAl can be calculated using the S-P rule as

$$m = [(0.5Z_{Co}) + (0.5Z_{Mn}) + Z_{Mn} + Z_{Al}] - 18, \quad (1)$$

where Z_i denotes the valence electrons of a single atom. Because Mn, Co, and Al have valence electron configurations of $3d^54s^2$, $3d^74s^2$, and $3s^23p^1$, respectively, Z_t tends to be

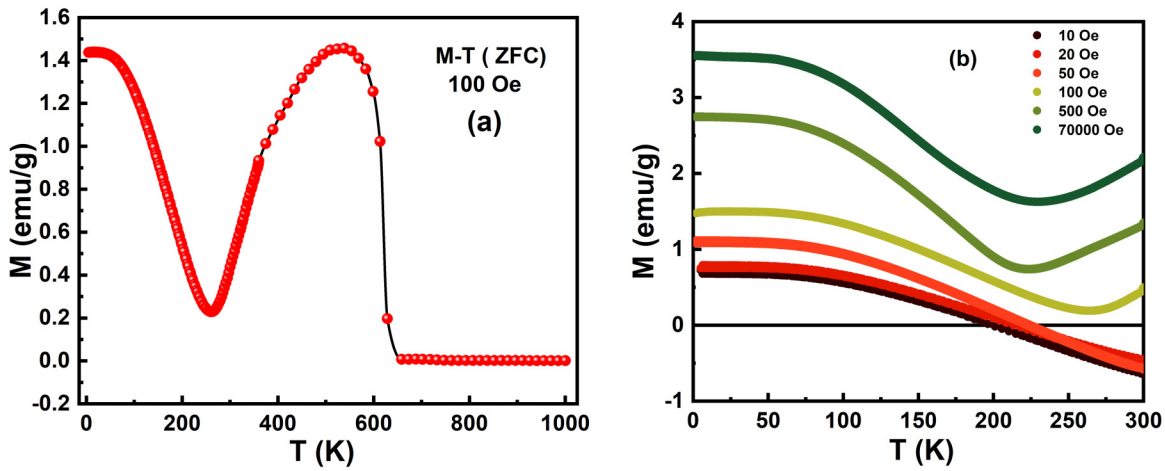

FIG. 3. Magnetization measured in (a) fields of 100 Oe depicting T_{com} along with T_C and (b) various fields as a function of temperature.

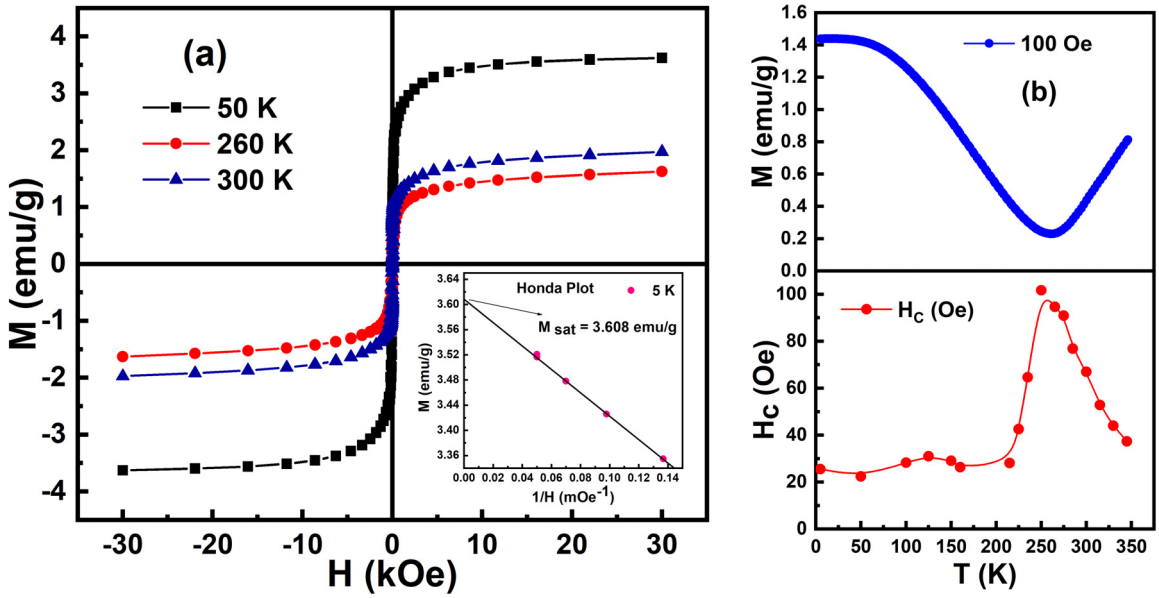

FIG. 4. (a) Magnetic hysteresis (*M-H* plot) at different temperatures. (b) The temperature variation of H_c near T_{com}. The inset of Fig. 4(a) depicts the Honda plot at 5 K.

the deciding number 18, which represents the FCFM state for half-Heusler systems. In light of this, the S-P rule predicts that $(Co_{0.5}Mn_{0.5})$MnAl should have a net moment of 0 μ_B/f.u. The magnetic hysteresis (*M-H*) measured at various temperatures in the field range −30 to +30 kOe (Fig. 4(a)) demonstrates a soft magnetic behavior with a low coercive field (H_C). The saturation magnetization (M_{sat}) obtained from the Honda plot [see inset of Fig. 4(a)] at 5 K was found to be 0.09 μ_B/f.u. (3.608 emu/g), which is quite close to the value calculated by applying the S-P rule. The little divergence observed might be attributed to the minor compositional variation. Based on the very small value of M_{sat} at temperatures other than T_{com}, it is possible to conclude that the sample virtually exhibits a magnetically compensated ferrimagnetic state throughout the range of temperatures. The temperature variation of the H_C derived from the *M-H* plot at different temperatures is shown in Fig. 4(b). The sample has a soft magnetic behavior with low coercivity throughout the temperature range. However, H_C increases toward the T_{com}, which is consistent with the Stoner-Wohlfarth model [23]. The H_C, according to this model, can be represented as

$$H_C = \frac{2K}{M_{sat}}, \tag{2}$$

where M_{sat} and K depict saturation magnetization and anisotropy constant, respectively. At T_{com}, the M_{sat} will be at its lowest, and H_C will exhibit a considerable increase toward T_{com} since it is inversely proportional to M_{sat}, as seen in Fig. 4(b).

Because the T_{com} of the compound is close to the ambient temperature, studying the behavior of the magnetocaloric effect (MCE) at the T_{com} is intriguing. By measuring the *M-H* plot around the T_{com}, the magnetocaloric characteristics of the compound were investigated. According to Maxwell's relation, the MCE can be expressed as

$$\Delta S_M(T,H) = \int_{H_i}^{H_f} \left(\frac{\partial M}{\partial T}\right)_H dH, \tag{3}$$

where M and T are the magnetic moment and temperature, respectively, and H denotes the magnetic fields [24]. Using the method mentioned above, we get the magnetic entropy change for a 10–70 kOe field change in the temperature range of 200–300 K, which is shown in Fig. 5. The value of MCE decreases with rising temperature and crosses the temperature axis at 225 K, turning negative. As a result, the sample exhibits a polarity reversal of $-\Delta S_M \sim 225$ K, with normal MCE $(-\Delta S_M > 0) < 225$ K and inverse MCE $(-\Delta S_M < 0) > 225$ K, as seen in Fig. 5. This polarity reversal happens at a temperature that perfectly matches the T_{com} (=225 K)

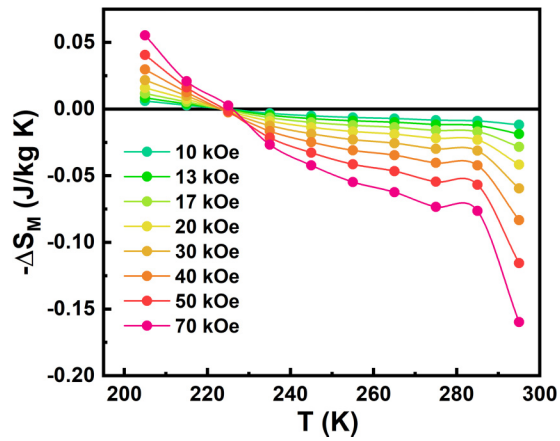

FIG. 5. Magnetic entropy $(-\Delta S_M)$ change with temperature for typical magnetic field changes estimated from *M-H* plots at different temperatures.

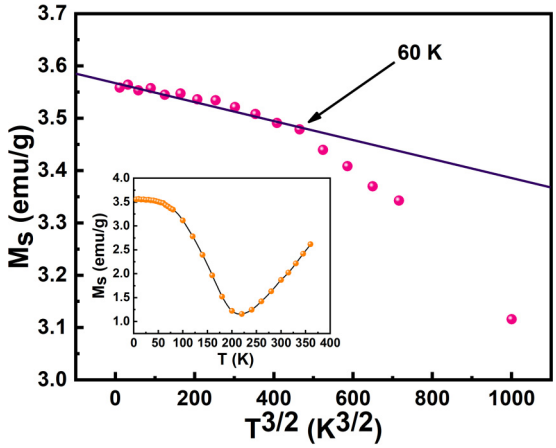

FIG. 6. The M_S vs $T^{3/2}$ plot along with the Bloch's law fit. Inset shows the temperature variation of spontaneous magnetization.

depicted in the temperature dependence of spontaneous magnetization (inset of Fig. 6). Magnetic refrigeration is achieved by the normal MCE, whereas magnetic heating is achieved by the inverse MCE [25,26]. Consequently, the system temperature is always kept distant from the vicinity of 225 K.

Since both Mn and Co are magnetic elements in $(Co_{0.5}Mn_{0.5})MnAl$, the observed magnetic compensation might be due to Mn and Co spin moments at different crystallographic locations. In the theoretical calculations of Ma *et al.* [18], the CoMnAl half-Heusler $C1_b$ structure was considered with Co, Mn, and Al atoms situated at Wyckoff positions $4c(\frac{1}{4}, \frac{1}{4}, \frac{1}{4})$, $4b(\frac{1}{2}, \frac{1}{2}, \frac{1}{2})$, and $4a(0, 0, 0)$, respectively, whereas the $4d(\frac{3}{4}, \frac{3}{4}, \frac{3}{4})$ position is vacant. Consequently, the Al and Mn atoms, which are positioned at 4*a* and 4*b* sites, respectively, will form a rock-salt structure arrangement, while the Co atom, which is positioned in the octahedrally coordinated pocket at one of the center 4*c* sites of the cube, will have a nearest-neighbor coordination made up of four Al atoms and four Mn atoms, which are spaced apart by $\sqrt{3}a/2$. The theoretical findings suggest that the magnetic moment value of the ferrimagnetically ordered CoMnAl compound is -0.25 and $1.38\mu_B$/f.u. for Co and Mn atoms, respectively [18]. Using the magnetic moment contributions from the Co, Mn, and Al atoms, the total magnetic moment for CoMnAl was estimated to be $1.04\mu_B/f.u.$. In $(Co_{0.5}Mn_{0.5})MnAl$, where the Mn atom replaces 50% of the Co atom, the Mn atom occupies positions 4*b* and 4*c* whereas the Co atom occupies position 4*c*. Generally, in Mn-based Heusler systems, the exchange coupling between the Mn moments is extremely sensitive to the variation in distance between the neighbors because of the Ruderman-Kittel-Kasuya-Yoshida (RKKY) exchange. This exchange mechanism incorporates the nearest-neighbor Mn-Mn interactions antiferromagnetically and the next-nearest-neighbor Mn-Mn interactions ferromagnetically. Because the Mn(4*c*)-Mn(4*b*) atom pair in $(Co_{0.5}Mn_{0.5})MnAl$ is located at the nearest-neighbor distance $\sqrt{3}a/4$, they are anticipated to couple antiferromagnetically as a result of the RKKY exchange, reducing the total magnetic moment of the compound. The computational calculation also demonstrates that the aforementioned magnetic configuration is the magnetic ground state of an ordered $(Co_{0.5}Mn_{0.5})MnAl$, which we shall address in detail later in the computational study.

Since spontaneous magnetization (M_S) and its temperature dependence are key quantities of relevance in the characterization of any specific magnetic phase, the magnetic isotherm method was used to assess its temperature dependency. It entails measuring the *M-H* at a specific temperature and then extrapolating the linear portion of the curve at the high field to zero field (Fig. 6). The inset of Fig. 6 shows the spontaneous magnetization variation with temperature. Below 60 K, the data were found to fit well to Bloch's law describing magnetization decay due to the spin-wave as

$$M_S(T) = M_S(0)[1 - BT^{3/2}], \tag{4}$$

where $M_S(0)$ depicts the spontaneous magnetization at 0 K, and B is the Bloch constant related to the T_C. The M_S vs $T^{3/2}$ plot along with Bloch's law fit is shown in Fig. 6. Hence, $<$ 60 K, it behaves like a local magnetic moment system, which is one of the necessary conditions for getting spin polarization in Heusler systems. This agrees with the prediction of the FSM calculation. However, when compared with magnetic splitting, the band gap responsible for high spin polarization in one of the spin channels may drop extremely fast with temperature, resulting in the gap vanishing far below the T_C [27–29]. Thus, the observed divergence from linearity in the M_S vs $T^{3/2}$ plot at 60 K suggests the likelihood of a drop in the band gap, which would result in electrons occupying the empty states near the E_F, reducing spin polarization from 100% at the E_F. Many other half-Heusler systems, such as NiMnSb [29], also showed a similar trend.

3. Neutron diffraction

To better understand the structural ordering and FCFM behavior, PND was performed at room temperature by exploiting the distinct scattering length for neutrons of the element. The quantitative study performed utilizing the Rietveld refinement method executed through the FULLPROF suite [30] reasserts the $F\bar{4}3m$ (216) crystal symmetry. The nuclear and magnetic phases have both been considered when PND data were refined. Scale, background, cell, moments on Co and Mn, and overall thermal parameters are among the altered parameters. Figure 7(a) depicts refinement fits for diffraction data at 300 K and reveals that the unit-cell parameter is 5.87 Å, consistent with the XRD data. Refinement of the data using the perfect $C1_b$ structure was considered first, but it generated a poor match to the experimental data. However, after including B2-type disorder in the system, we found good agreement between the recorded data and the calculated profile [Fig. 7(a)], with relatively better fitting parameters. In a half-Heusler system with B2-type disorder, the 4*a* site is equivalent to the 4*b* site, and the 4*c* site is equivalent to the 4*d* site [13]. Thus, for this sort of crystallographic arrangement, Mn and Al share 4*a* and 4*b* sites, while a sizable fraction of substituted Mn moves from the 4*c* site to the unoccupied 4*d* site, leaving Co, Mn, and voids at the 4*c* site. This antisite disorder lacks complete intermixing but has a favored occupation, as shown in Fig. 7(b). The proposed model is feasible for two reasons. First, the Mn-Al disorder has been seen in various Heusler compounds such as Mn_2CoAl [31,32]. Second,

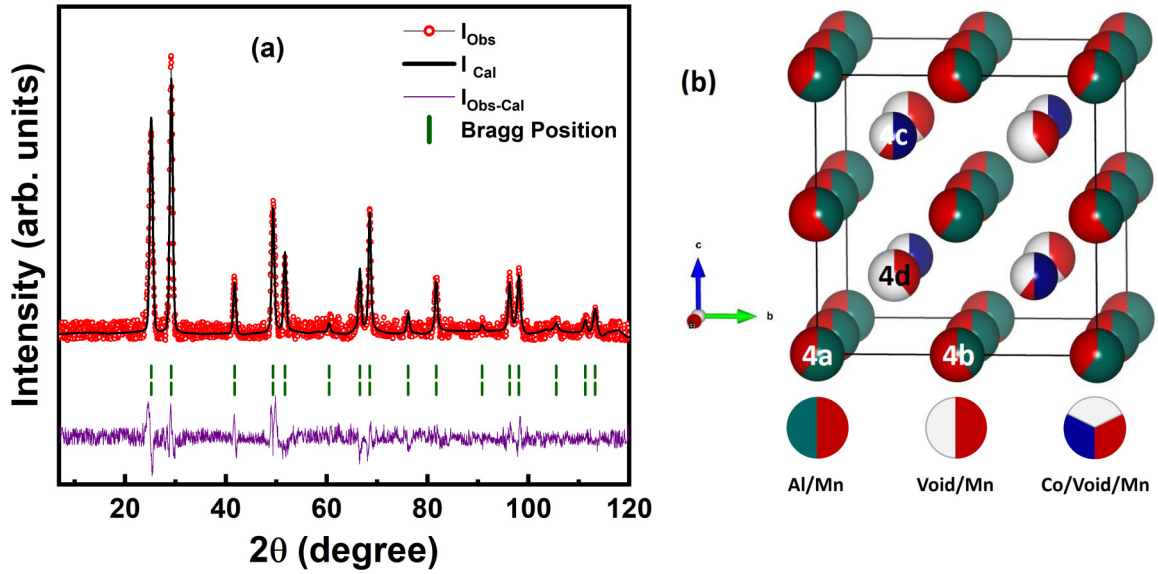

FIG. 7. (a) Neutron diffraction data of $(Co_{0.5}Mn_{0.5})MnAl$ measured at room temperature along with the Rietveld refinement fit considering the structure as depicted in (b).

the Mn atom that moves to the void at the 4*d* site while leaving considerably bigger Co at the 4*c* site might be considered to lower local stress. A similar intermixing of atoms with void can be observed in other half-Heusler compounds, such as IrMnGa [33]. The analysis has shown that the magnetic structure is a FCFM, with a site-specific magnetic moment stated in Table I, consistent with the findings of magnetic studies.

As depicted in Fig. 7(b), the $(Co_{0.5}Mn_{0.5})MnAl$ can be considered a layered structure, where Mn(4*a*)-Al(4*a*)/Mn(4*b*)-Al(4*b*) layers and Co(4*c*)-Mn(4*c*)/Mn(4*d*) layers sandwich each other with a distance of $\frac{1}{4}$ of the lattice parameter. Here, the Mn(4*a*)-Al(4*a*)/Mn(4*b*)-Al(4*b*) layer exhibits a negative net moment, while the Co(4*c*)-Mn(4*c*)/Mn(4*d*) layer exhibits a positive net moment, resulting in a completely compensated ferrimagnetic state in the system. Because Mn and Co are the only magnetic elements in $(Co_{0.5}Mn_{0.5})MnAl$, the arrangement of the Mn and Co atoms completely dictates the magnetic characteristics of the compound. Furthermore, because of the oscillatory RKKY exchange, the Mn-moment coupling is particularly sensitive to how far away their next neighbors are, and it may either be positive or negative based on how far apart moments are. Since Mn is present at all possible Wyckoff positions due to B2-type disorder in the system, we could observe randomness in coupling between Mn atoms at the nearest-neighbor distance. The Mn atom at 4*a*, for example, couples antiferromagnetically with Mn at 4*c*, whereas Mn at 4*b* couples ferromagnetically with Mn at 4*c*, despite having a nearest-neighbor distance. This randomness in coupling may be induced by the distribution of nonmagnetic Al atoms and the voids at different Wyckoff positions, causing the distance to the nearest and next-nearest Mn neighbors to change at random.

TABLE I. The estimated site-specific magnetic moment results from neutron analysis.

	Site-specific magnetic moment (μ_B/atom)	
Wyckoff position	Mn	Co
4*a*	−0.543	–
4*c*	0.101	0.148
4*b*	0.051	–
4*d*	0.409	–
M_{Total} (ND) = 0.166 μ_B/f.u.		

4. *Electrical transport*

Figure 8(a) depicts the resistivity (ρ) behavior of the compound, which exhibits characteristics like that of a semiconductor with a negative temperature coefficient. The absence of exponential dependency, on the other hand, rules out the possibility of gapped semiconducting nature. As a result, the material may be a gapless semiconductor, a spin-gapless semiconductor, or a semimetal. To better understand this behavior, a two-carrier model is used to examine the conductivity (σ) in the temperature range of 100–300 K. According to this model the total conductivity can be written as

$$\sigma = \sigma_e + \sigma_h = en_e\mu_e + en_h\mu_h, \tag{5}$$

where $n_i = n_{i0}\exp(-\frac{\Delta E_i}{k_B T})$ $(i = e, h)$ represents the carrier concentrations with mobilities μ_i and energy gap ΔE_i. The mobilities are determined by $\mu_i = \frac{1}{\alpha_i T + \beta_i}$ $(i = e, h)$, where α and β terms correspond to electron-phonon scattering and mobility due to defect at 0 K, respectively. Hence, the total conductivity can be written as

$$\sigma(T) = A(T)\exp\left(-\frac{\Delta E_e}{k_B T}\right) + B(T)\exp\left(-\frac{\Delta E_h}{k_B T}\right), \tag{6}$$

where $A(T) = \frac{en_{e0}\mu_{e0}}{1+\alpha_e' T}$ and $B(T) = \frac{en_{h0}\mu_{h0}}{1+\alpha_h' T}$. Figure 8(b) displays the σ vs T plot along with the fit, and the energy gaps revealed by the fit are 0.3 and 3 meV. Since holes comprise

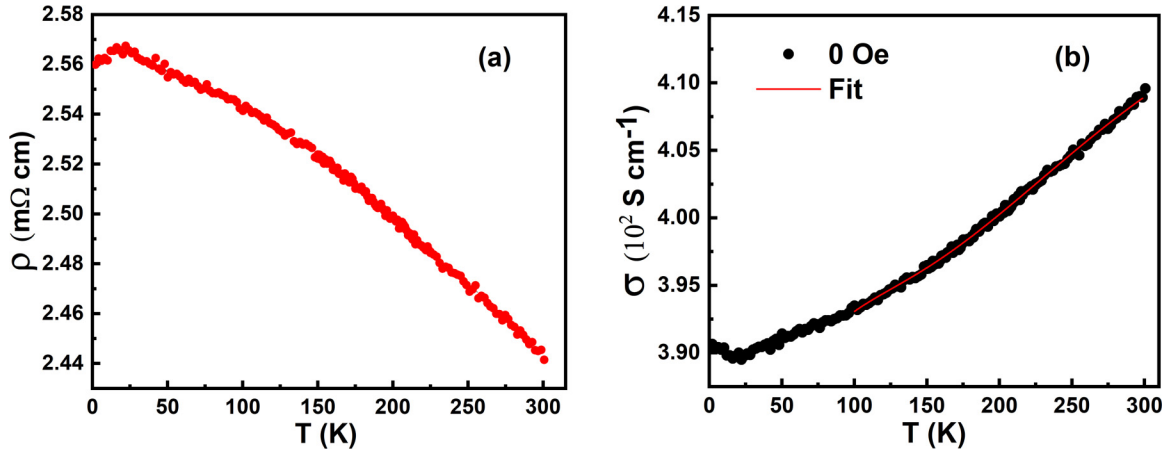

FIG. 8. Temperature variation of (a) electrical resistivity and (b) electrical conductivity along with the fit using two-carrier model for $(Co_{0.5}Mn_{0.5})MnAl$.

most carriers according to Hall effect measurements, the lower-energy gap is attributed to them.

5. Hall effect measurement

The *M-T* and *M-H* measurements only offer a hint of sublattice spin-crossing at the compensation point. Because the Hall effect is an intriguing quantity for direct observation of the sublattice-spin crossover, measurements at various temperatures were done, as shown in Fig. 9.

To ensure consistency, the Hall effect and magnetization experiments were carried out on the same sample at the same temperatures and field orientations. To eliminate any longitudinal component of the resistivity, the average of the positive and negative field Hall resistivity (ρ_{xy}) values were employed. The ρ_{xy} vs H plot was found to behave like the *M-H* plot at various temperatures. The ρ_{xy} grows with increasing magnetic field in the low-field regime and reaches saturation > 15 kOe. In addition to the ordinary Hall effect, a ferromagnet has another contribution proportional to magnetization known as anomalous Hall resistivity. This extra contribution can be attributed to the asymmetric scattering of electrons carrying current. The empirical equation for ρ_{xy} may thus be expressed as

$$\rho_{xy} = R_0 H + R_{\mathrm{AH}} M, \tag{7}$$

where R_0 and R_{AH} depict the coefficient of ordinary and anomalous Hall resistivity, respectively. In this case, the R_0 is determined by the relationship $R_0 = \pm\frac{1}{ne}$, which depends on the kind of carriers (electrons or holes) and their density (n). The R_0, which was determined from the linear fit of high-field data at 300 K, was found to be $3.64(\times 10^{-6}\mu\Omega\,\mathrm{cm/Oe})$, which is in the same order of magnitude as in the case of semimetallic full-Heusler Fe_2TiAl [34]. The fact that R_0 is positive means that holes are the main charge carriers. To calculate anomalous Hall resistivity, the y intercept of the extrapolated linear fit at the high-magnetic-field region is employed. Below T_{com} [Fig. 9(a)], the anomalous Hall effect was found to exhibit a negative sign, i.e., negative (positive) value in the positive (negative) field, whereas above T_{com} [Fig. 9(b)], the anomalous Hall effect exhibits a positive value. Since the anomalous Hall resistivity is proportional to the magnetization according to Eq. (7), its sign change ~ 200 K, where the magnetization was found to be absolutely zero, is expected. This sign change of the anomalous Hall effect, as seen in

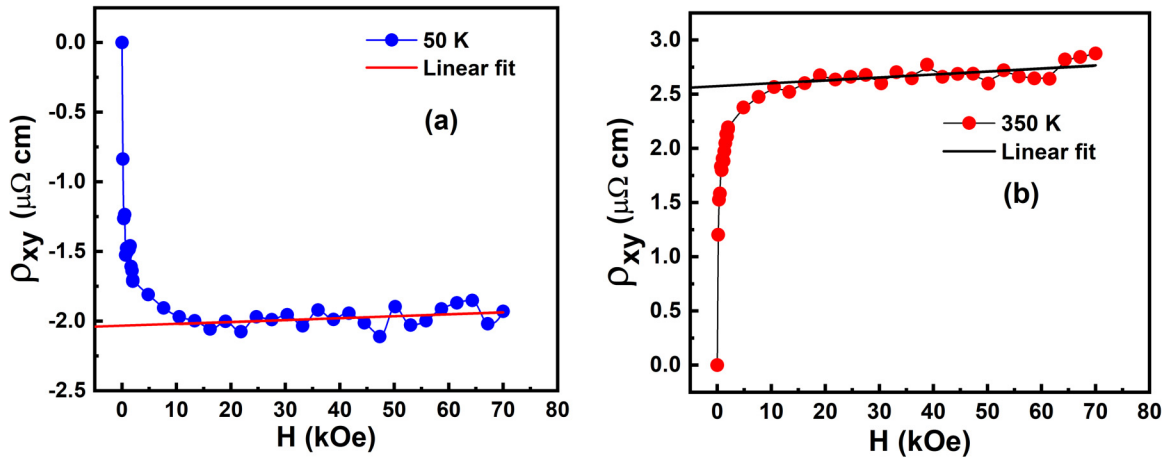

FIG. 9. Field dependency of the Hall resistivity (ρ_{xy}) measured at (a) 50 K and (b) 350 K.

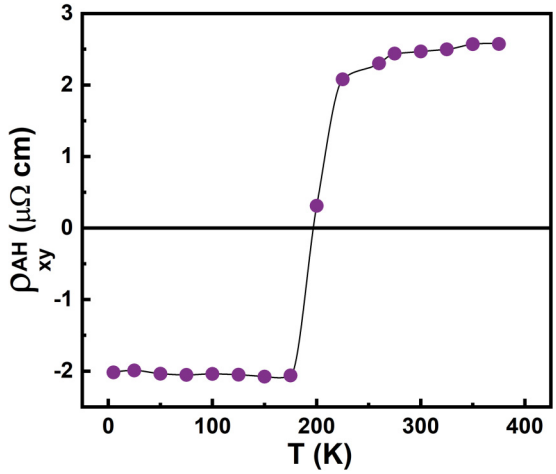

FIG. 10. Temperature variation of anomalous Hall resistivity calculated via extrapolated high field linear fit.

Fig. 10, shows that the sublattice magnetic structure changes across T_{com}. A comparable situation has been observed in some other magnetically compensated Heusler compounds, including $Mn_{1.5}V_{0.5}FeAl$ [21] and Mn_2Ru_xGa [22].

6. Thermal transports

The Seebeck coefficient (S) is a sensitive probe of electronic band structure around E_F. This led to measuring its temperature dependence in the range of 2–400 K, as depicted in Fig. 11. The compound has a positive S value which varies with temperature and exhibits a broad maximum ~ 200 K followed by a crossover to negative values > 360 K, indicating that both electrons and holes affect the total S. When both carriers are involved in the process, the total S can be represented as

$$S = \frac{S_e\sigma_e + S_h\sigma_h}{\sigma_e + \sigma_h}, \tag{8}$$

with $S_e < 0$ and $S_h > 0$, where S_i and σ_i represents the Seebeck coefficient and conductivities of electrons and holes, respectively [35]. At low temperatures, there is just one sort

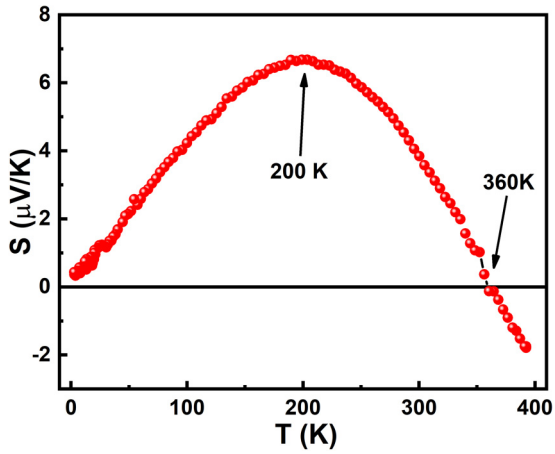

FIG. 11. Temperature variation of Seebeck coefficient (S) in the range 2–400 K.

of carrier that contributes to the S (extrinsic region). Accordingly, when the temperature rises, $|S|$ first increases and then reaches a maximum ($|S|_{max}$, T_{max}) as the other type of carriers begin to substantially participate (bipolar/intrinsic region). These characteristics are quite evident in Fig. 11, where the broad maximum of ~ 200 K may be due to the contribution of thermally excited carriers across the pseudogap. The result of the Hall effect measurements is compatible with the positive value of S, which in the temperature range of 2–360 K suggests that most carriers are of the hole type. We attribute the observation of a very low value of the S ($S < 10\,\mu V/K$) to the formation of the compensatory electron and hole pockets (see Fig. 12, right panel), as discussed in the next section. This behavior differs from that of ordinary semiconductors, which are noted for having high S values. A similar trend of low S values and broad maxima was also reported in other Heusler compounds, such as Mn_2CoAl [36], Ru_2TaAl [37], Fe_2VAl [38], and MNiSn(M = Zr, Hf) [39]. These features might support the semimetallic nature of $(Co_{0.5}Mn_{0.5})$MnAl.

B. Theoretical results

To gain theoretical insight to the predicted SSM phase, the first-principles electronic structure calculations were performed on the ordered $(Co_{0.5}Mn_{0.5})$MnAl using the experimentally obtained structural parameters and within the framework of DFT. For this purpose, the full-potential linearized augmented plane-wave method, as implemented in the WIEN2K code [40], is employed. To approximate the exchange-correlation energy, the generalized gradient approximation functional of Perdew-Burke-Ernzerhof is used [41]. For the Brillouin zone integration, denser Monkhorst-Pack grids ($8 \times 8 \times 8$) are considered, which yield 260 k points in the irreducible Brillouin zone [42]. The energy convergence criterion for total energy and total charge density is set to 10^{-4} Ry. As already mentioned, our experimental results suggest that $(Co_{0.5}Mn_{0.5})$MnAl exhibits a very low M_{sat} of 0.09 μ_B /f.u., which indicates a compensatory ferrimagnetic configuration. The variation of total energy and local spin moment (LSM) distributions of Co, Mn_I (the substituting Mn), and Mn_{II} sublattices as a function of FSM per formula unit is shown in Fig. 13. Here, E_0 represents the total energy corresponding to FSM = 0. The important inferences made from this figure are as follows: (i) The energy increases monotonically with FSM, which agrees well with the experimental observation of a very low saturation moment. (ii) As far as the magnetic ordering is concerned [see Fig. 13(b) and inset], Co and the substituent Mn_I occupy the 4c position and couple ferromagnetically while they are oriented antiparallel to the Mn_{II} occupying the 4b position. However, the strength of magnetization for each of them varies to give a net compensated magnetic moment. The site-specific spin polarization is maximum at Mn_I followed by Mn_{II} and Co. Furthermore, the increase in FSM results in rapid weakening of the polarization at the Mn_{II} site.

To provide insight into the electronic structure that leads to the compensating ferrimagnetic ordering, we have investigated the electronic properties of the ground state magnetic order of $(Co_{0.5}Mn_{0.5})$MnAl. A basic understanding of the symmetry of the lattice will help in explaining the

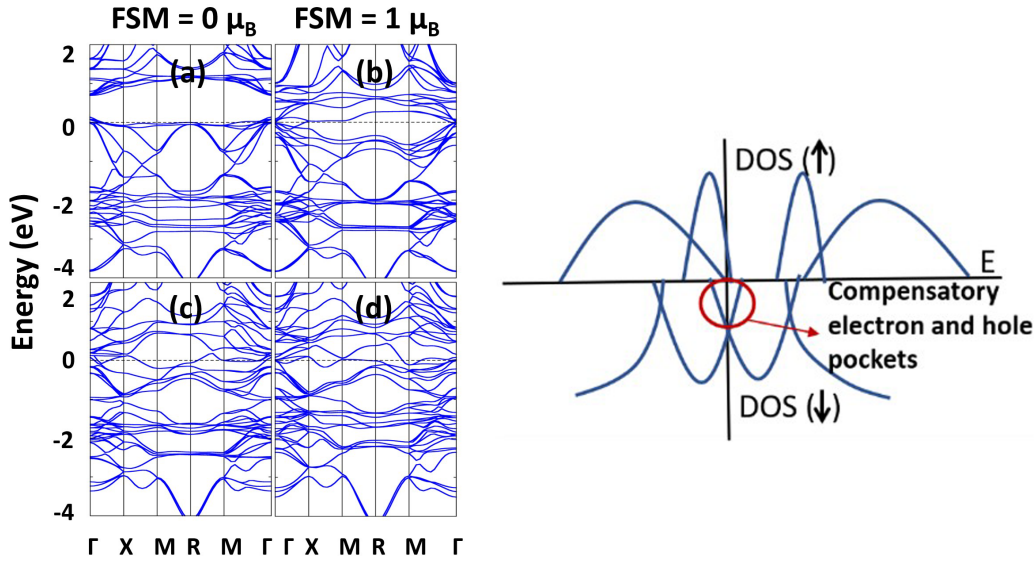

FIG. 12. (Left panel) (a) and (b) Spin-up and (c) and (d) spin-down band structures for fixed spin moment (FSM) = 0 and 1 μ_B, respectively. (Right panel) Schematic illustration of the spin and subband resolved density of states (DOS) for FSM = 0.

electronic structure. In this compound, due to the lack of charge transfer as in the case of oxides, none of the constituents behaves like a cation or anion. The electronic redistribution happens only through covalent bonding. While Mn_{II} and Al form a cubic symmetry to favor axial e_g-p interactions, Co/Mn_I favors t_{2g}-p interaction with Al. In addition to these primary interactions, there are varieties of second neighbor d-d, p-p interactions which determine the electronic structure of the system. Furthermore, a large spin-exchange split of the partially occupied d states creates a LSM and in turn stabilizes the magnetic ground state. The atom and orbital resolved DOS shown in Fig. 14 summarize the above. From Fig. 14, we gather that the Mn and Co 4s states are completely empty, while Al 3p states are less than half occupied. Therefore, one can nominally assign $3d^{9-\delta_1}$, $3d^{7-\delta_2}$, $3d^{7-\delta_3}$, and $3p^{(1+\delta_1+\delta_2+\delta_3)}$ oxidation states for Co, Mn_I, Mn_{II}, and Al, respectively. The fractional numbers δ_1, δ_2, and δ_3 are due to the covalent hybridizations, as discussed above. Further analysis of the orbital occupancies in both spin channels reveals the following spin-polarized electronic configurations. In the case of FSM = 0, we have Co-$3d^{(5-\delta_1)\uparrow,\,(4+\delta_1)\downarrow}$, Mn_I-$3d^{(5-\delta_2)\uparrow,\,(2+\delta_2)\downarrow}$, and Mn_{II}-$3d^{(2+\delta_3)\uparrow,\,(5-\delta_3)\downarrow}$. In the case of FSM = 1, we have Co-$3d^{(5-\delta_1)\uparrow,\,(4+\delta_1)\downarrow}$, Mn_I-$3d^{(5-\delta_2)\uparrow,\,(2+\delta_2)\downarrow}$, and Mn_{II}-$3d^{(2+\delta_3)\uparrow,\,(5-\delta_3)\downarrow}$, which agree well with the DFT-calculated LSMs for Co, Mn_I, and Mn_{II}, which are 1.09 (1.12), 3.07(2.65), and −2.34 (−1.02) μ_B, respectively, corresponding to FSM = 0 (FSM = 1) μ_B. The δ's add minor variation to the spin distributions due to several factors including induced magnetization of the Al p

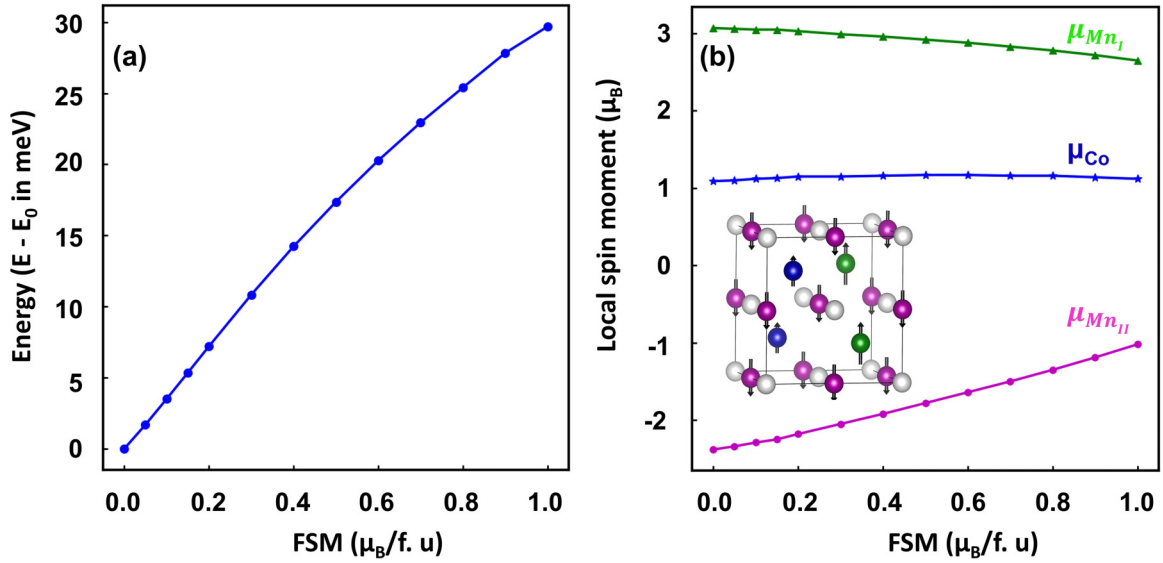

FIG. 13. (a) The total energy and (b) the local moments of Co (blue), Mn_I (green), and Mn_{II} (magenta) sublattices as a function of fixed spin moment (FSM).

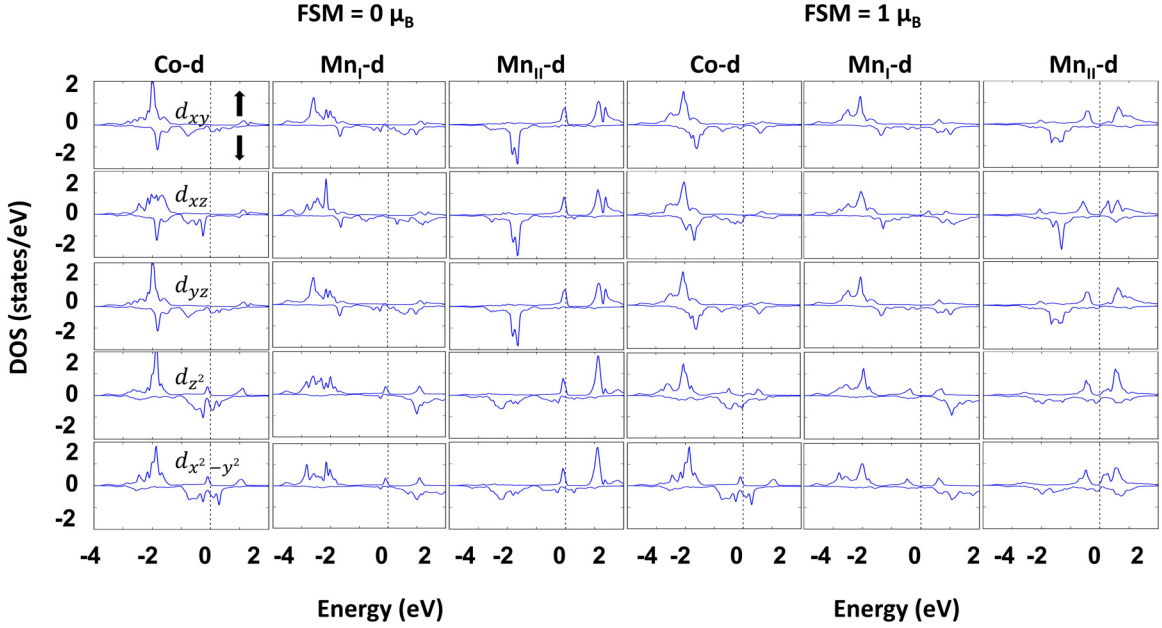

FIG. 14. The atom-resolved density of states (DOS) for Co, Mn_I, and Mn_{II} d orbitals. The up and down arrows indicate spin-up and spin-down DOS.

states. These are not necessarily to be exactly determined. As we move from FSM = 0 to 1 μ_B, the increase in the magnetic moment is accompanied by a decrease in the magnetization at the Mn_{II} site, which can be explained by the band structure plotted in Fig. 12. One of the nearly three degenerate bands lying on the E_F in the spin-up channel for FSM = 0 moves up and becomes unoccupied for FSM = 1 μ_B. As the orbital projected DOS reveals, this band is primarily formed by the Mn_{II} d states (see Figs. S2–S7 in the Supplemental Material [43]). The shift of the band in the spin-up channel leads to electron occupancy reshuffling in the spin-down channel. Authors of earlier studies on the pristine CoMnAl [18], also verified by us, have reported that the LSMs for Co and Mn (the same as Mn_{II} for the present compound) are 1.04 and -0.25 μ_B, respectively. The substitution has enhanced the magnetization at each atomic site while maintaining the site-specific magnetic order. This is anti-intuitive if one follows the S-P curve for a half-Heusler compound, where it is suggested that, if the total valence electron count is 18, then a band gap emerges at E_F, and the system stabilizes in a paramagnetic/nonmagnetic state [5,6]. However, while $(Co_{0.5}Mn_{0.5})$MnAl has a valence electron count of 18, in the nonmagnetic configuration, it does not exhibit a band gap (see Fig. S1 in the Supplemental Material [43]). Also, we find that the nonmagnetic state is energetically higher than the FSM = 0 state by ∼394.75 meV/f.u. The substitution at the 4c site breaks the point group symmetry, and the corresponding disorder introduces localization through the less dispersive states at E_F. The localization gives rise to the magnetization. Interestingly, the magnetization has increased the LSM at both 4b (Mn_{II}) and 4c (through Mn_I). Since both are compensating in nature, one notices zero magnetic moment or low saturation moment. The present analysis suggests that one can tune the saturation magnetic moment through the substitutional Mn concentration, which is significant in the context of spintronics applications. Furthermore, the low saturation magnetic moment of the system creates a SSM quantum phase [1], as shown in the schematically depicted spin and subband resolved DOS (right panel of Fig. 12), with a spin polarization (p) of 42% quantified at E_F using the relation $p(= \frac{D_\uparrow - D_\downarrow}{D_\uparrow + D_\downarrow} \times 100)$, which is significant in the context of spintronics applications. Here, $D_\uparrow$ and $D_\downarrow$ stand for the densities of spin-up and spin-down states at E_F, respectively.

IV. SUMMARY AND CONCLUSION

The realization of a completely compensated ferrimagnetic state on a cubic half-Heusler structure ($C1_b$) has been the subject of various theoretical reports; however, none of these reported compounds were formed in the desired crystal structure. In this paper, a half-Heusler compound $(Co_{0.5}Mn_{0.5})$MnAl is proposed and synthesized successfully in the cubic ($C1_b$) structure. The theoretical and experimental investigation infers a FCFM and SSM quantum phase. The electronic structure analysis for the experimentally observed FCFM phase ($0.09\mu_B$/f.u. at 5 K) was performed using FSM calculation within the framework of DFT and observed a SSM quantum phase, which is in excellent agreement with the transport studies of resistivity and Seebeck coefficient measurements. The T_C of 634 K was observed, making it appropriate for room-temperature applications. Additionally, Néel N-type ferrimagnetic behavior with temperature-dependent sublattice spin crossover across the T_{com} was inferred from the magnetic data and validated by the Hall resistivity measurements. In conclusion, the presence of interesting features in $(Co_{0.5}Mn_{0.5})$MnAl, such as high T_C, magnetic moment compensation, and spin polarization, makes this material appealing for spintronic device applications.

ACKNOWLEDGMENTS

R.H. and H.K.N. would like to acknowledge DST FIST-Phase II funding for the PPMS facility used for this paper (SR/FST/PSII-038/2016). The authors acknowledge IIT-Madras for the financial assistance for the SVSM facility. Also, the authors would like to acknowledge HPCE at IIT Madras for providing computing resources. This paper is funded by the Department of Science and Technology, India, through Grant No. CRG/2020/004330.

[1] Y. Venkateswara, S. S. Samatham, P. D. Babu, K. G. Suresh, and A. Alam, Co-existence of spin semi-metallic and Weyl semi-metallic behavior in FeRhCrGe, Phys. Rev. B **100**, 180404(R) (2019).

[2] J. Nag, D. Rani, D. Singh, R. Venkatesh, B. Sahni, A. K. Yadav, S. N. Jha, D. Bhattacharyya, P. D. Babu, K. G. Suresh *et al.*, CoFeVSb: A promising candidate for spin valve and thermoelectric applications, Phys. Rev. B **105**, 144409 (2022).

[3] T. Hadji, H. Khalfoun, H. Rached, and A. Azzouz-Rached, Spin gapless semiconductor and nearly spin semimetal antiferromagnets: The case of the inverse Heusler compounds Mn_2LiZ ($Z = $ Al and Ga), Mater. Res. Bull. **143**, 111461 (2021).

[4] M. Baral and A. Chakrabarti, Half-metallicity versus symmetry in half-Heusler alloys based on Pt, Ni, and Co: An *ab initio* study, Phys. Rev. B **99**, 205136 (2019).

[5] I. Galanakis, P. H. Dederichs, and N. Papanikolaou, Slater-Pauling behavior and origin of the half-metallicity of the full-Heusler alloys, Phys. Rev. B **66**, 174429 (2002).

[6] B. R. K. Nanda and I. Dasgupta, Electronic structure and magnetism in half-Heusler compounds, J. Phys.: Conden. Matter **15**, 7307 (2003).

[7] H. Van Leuken and R. A. De Groot, Half-Metallic Antiferromagnets, Phys. Rev. Lett. **74**, 1171 (1995).

[8] R. A. de Groot, Half-metallic magnetism in the 1990s, Phys. B: Condens. Matter **172**, 45 (1991).

[9] M. Bode, Spin-polarized scanning tunnelling microscopy, Rep. Prog. Phys. **66**, 523 (2003).

[10] C. D. Stanciu, A. Tsukamoto, A. V. Kimel, F. Hansteen, A. Kirilyuk, A. Itoh, and Th. Rasing, Subpicosecond Magnetization Reversal Across Ferrimagnetic Compensation Points, Phys. Rev. Lett. **99**, 217204 (2007).

[11] M. Fiebig, N. P. Duong, T. Satoh, B. B. Van Aken, K. Miyano, Y. Tomioka, and Y. Tokura, Ultrafast magnetization dynamics of antiferromagnetic compounds, J. Phys. D: Appl. Phys. **41**, 164005 (2008).

[12] W. E. Pickett, Single Spin Superconductivity, Phys. Rev. Lett. **77**, 3185 (1996).

[13] T. Graf, C. Felser, and S. S. P. Parkin, Simple rules for the understanding of Heusler compounds, Prog. Solid State Chem. **39**, 1 (2011).

[14] Y. J. Zhang, Z. H. Liu, Z. G. Wu, and X. Q. Ma, Prediction of fully compensated ferrimagnetic spin-gapless semiconducting FeMnGa/Al/In half Heusler alloys, IUCrJ **6**, 610 (2019).

[15] Y. J. Zhang, Z. H. Liu, G. D. Liu, and X. Q. Ma, Half-metallic fully compensated ferrimagnetism in $C1_b$-type half Heusler compounds $Mn_2Si_{1-x}Ge_x$, J. Magn. Magn. Mater **387**, 67 (2015).

[16] H. Z. Luo, G. D. Liu, F. B. Meng, W. H. Wang, G. H. Wu, X. X. Zhu, and C. B. Jiang, Half-metallicity and magnetic properties of half-Heusler type Mn_2Sn: *Ab initio* predictions, Phys. B: Conden. Matter **406**, 4245 (2011).

[17] Z. Cui, H. Ding, K. Xu, and Y. Feng, Electronic structures of various (001) and (111) surfaces, interfaces and spin transport properties of half-metallic fully compensated ferrimagnet Cr_2Se, J. Alloys. Compd. **884**, 161089 (2021).

[18] J. Ma, V. I. Hegde, K. Munira, Y. Xie, S. Keshavarz, D. T. Mildebrath, C. Wolverton, A. W. Ghosh, and W. H. Butler, Computational investigation of half-Heusler compounds for spintronics applications, Phys. Rev. B **95**, 024411 (2017).

[19] L. Néel, Magnetism and local molecular field, Science **174**, 985 (1971).

[20] A. Kumar and S. M. Yusuf, The phenomenon of negative magnetization and its implications, Phys. Rep. **556**, 1 (2015).

[21] R. Stinshoff, A. K. Nayak, G. H. Fecher, B. Balke, S. Ouardi, Y. Skourski, T. Nakamura, and C. Felser, Completely compensated ferrimagnetism and sublattice spin crossing in the half-metallic Heusler compound $Mn_{1.5}FeV_{0.5}Al$, Phys. Rev. B **95**, 060410(R) (2017).

[22] C. Fowley, K. Rode, Y.-C. Lau, N. Thiyagarajah, D. Betto, K. Borisov, G. Atcheson, E. Kampert, Z. Wang, Y. Yuan *et al.*, Magnetocrystalline anisotropy and exchange probed by high-field anomalous Hall effect in fully compensated half-metallic Mn_2Ru_xGa thin films, Phys. Rev. B **98**, 220406(R) (2018).

[23] S.-i. Ohkoshi, T. Iyoda, A. Fujishima, and K. Hashimoto, Magnetic properties of mixed ferro-ferrimagnets composed of Prussian blue analogs, Phys. Rev. B **56**, 11642 (1997).

[24] V. K. Pecharsky and K. A. Gschneidner, Magnetocaloric effect and magnetic refrigeration, J. Magn. Magn. Mater **200**, 44 (1999).

[25] S. M. Yusuf, A. Kumar, and J. V. Yakhmi, Temperature- and magnetic-field-controlled magnetic pole reversal in a molecular magnetic compound, Appl. Phys. Lett. **95**, 182506 (2009).

[26] L. H. Yin, Y. Liu, S. G. Tan, B. C. Zhao, J. M. Dai, W. H. Song, and Y. P. Sun, Multiple temperature-induced magnetization reversals in $SmCr_{1-x}Fe_xO_3$ system, Mater. Res. Bull. **48**, 4016 (2013).

[27] C. Hordequin, D. Ristoiu, L. Ranno, and J. Pierre, On the cross-over from half-metal to normal ferromagnet in NiMnSb, Eur. Phys. J. B **16**, 287 (2000).

[28] M. Zhang, E. Brück, F. R. de Boer, Z. Li, and G. Wu, The magnetic and transport properties of the Co_2FeGa Heusler alloy, J. Phys. D: Appl. Phys. **37**, 2049 (2004).

[29] C. Hordequin, J. Pierre, and R. Currat, Magnetic Excitations in the Half-Metallic NiMnSb Ferromagnet: From Heisenberg-Type to Itinerant Behaviour, J. Magn. Magn. Mater. **162**, 75 (1996).

[30] J. Rodríguez-Carvajal, Recent advances in magnetic structure determination by neutron powder diffraction, Phys. B: Condens Matter **192**, 55 (1993).

[31] X. D. Xu, Z. X. Chen, Y. Sakuraba, A. Perumal, K. Masnda, L. S. R. Kumara, H. Tajiri, T. Nakatani, J. Wang, W. Zhou *et al.*, Microstructure, magnetic and transport properties of a Mn_2CoAl Heusler compound, Acta Mater. **176**, 33 (2019).

[32] Z. Chen, W. Liu, P. Chen, X. Ruan, J. Sun, R. Liu, C. Gao, J. Du, B. Liu, H. Meng *et al.*, Direct observation of ferrimagnetic ordering in inverse Heusler alloy Mn_2CoAl, Appl. Phys. Lett. **117**, 012401 (2020).

[33] J. Kroder, K. Manna, D. Kriegner, A. S. Sukhanov, E. Liu, H. Borrmann, A. Hoser, J. Gooth, W. Schnelle, D. S. Inosov *et al.*, Spin glass behavior in the disordered half-Heusler compound IrMnGa, Phys. Rev. B **99**, 174410 (2019).

[34] N. I. Kourov, V. V. Marchenkov, K. A. Belozerova, and H. W. Weber, Galvanomagnetic properties of Fe_2YZ (Y = Ti, V, Cr, Mn, Fe, Ni; Z = Al, Si) Heusler alloys, J. Exp. Theor. Phys. **121**, 844 (2015).

[35] A. N. Gandi and U. Schwingenschlögl, Electron dominated thermoelectric response in *M*NiSn (*M*: Ti, Zr, Hf) half-Heusler alloys, Phys. Chem. Chem. Phys. **18**, 14017 (2016).

[36] S. Ouardi, G. H. Fecher, and C. Felser, Realization of Spin Gapless Semiconductors: The Heusler Compound Mn_2CoAl, Phys. Rev. Lett. **110**, 100401 (2013).

[37] C. W. Tseng, C. N. Kuo, H. W. Lee, K. F. Chen, R. C. Huang, C. M. Wei, Y. K. Kuo, and C. S. Lue, Semimetallic behavior in Heusler-type Ru_2TaAl and thermoelectric performance improved by off-stoichiometry, Phys. Rev. B **96**, 125106 (2017).

[38] Y. Nishino, H. Kato, M. Kato, and U. Mizutani, Effect of off-stoichiometry on the transport properties of the Heusler- type Fe_2 VAl compound, Phys. Rev. B **63**, 233303 (2001).

[39] T. Kanemitsu, H. Muta, K. Kurosaki, and S. Yamanaka, Transport properties of niobium doped *M*NiSn (M= Ti, Zr), 2006 25th International Conference on Thermoelectrics (IEEE, Vienna, 2006).

[40] D. R. Hamann, Semiconductor Charge Densities with Hard-Core and Soft-Core Pseudopotentials, Phys. Rev. Lett. **42**, 662 (1979).

[41] J. P. Perdew, K. Burke, and M. Ernzerhof, Generalized Gradient Approximation Made Simple, Phys. Rev. Lett. **77**, 3865 (1996).

[42] J. D. Pack and H. J. Monkhorst, "Special points for Brillouin-zone integrations"—A reply, Phys. Rev. B **16**, 1748 (1977).

[43] See Supplemental Material at http://link.aps.org/supplemental/10.1103/PhysRevB.108.094407 for more details on non-magnetic, orbital resolved band structures of Co, Mn_I, Mn_{II} for FSM = 0 and FSM =1 μ_B.